Research article

Chang-Wei Cheng, Soniya S. Raja, Ching-Wen Chang, Xin-Quan Zhang, Po-Yen Liu, Yi-Hsien Lee, Chih-Kang Shih and Shangjr Gwo*

Epitaxial aluminum plasmonics covering full visible spectrum

https://doi.org/10.1515/nanoph-2020-0402
Received July 19, 2020; accepted September 18, 2020; published online November 25, 2020

Abstract: Aluminum has attracted a great deal of attention as an alternative plasmonic material to silver and gold because of its natural abundance on Earth, material stability, unique spectral capability in the ultraviolet spectral region, and complementary metal-oxide-semiconductor compatibility. Surprisingly, in some recent studies, aluminum has been reported to outperform silver in the visible range due to its superior surface and interface properties. Here, we demonstrate excellent structural and optical properties measured for aluminum epitaxial films grown on sapphire substrates by molecular-beam epitaxy under ultrahigh vacuum growth conditions. Using the epitaxial growth technique, distinct advantages can be achieved for plasmonic applications, including high-fidelity nanofabrication and wafer-scale system integration. Moreover, the aluminum film thickness is controllable down to a few atomic monolayers, allowing for plasmonic ultrathin layer devices. Two kinds of aluminum plasmonic applications are reported here, including precisely engineered plasmonic substrates for surface-enhanced Raman spectroscopy and high-quality-factor plasmonic surface lattices based on standing localized surface plasmons and propagating surface plasmon polaritons, respectively, in the entire visible spectrum (400–700 nm).

Keywords: aluminum epitaxial film; molecular-beam epitaxy; monolayer transition metal dichalcogenide; plasmonic surface lattice; surface-enhanced Raman spectroscopy; surface plasmon interferometry.

1 Introduction

Plasmonics is a rapidly evolving field that takes advantage of strong light confinement and drastically enhanced light–matter interactions beyond the diffraction limit near the surfaces and interfaces of metal nanostructures. In the past few decades, remarkable advances based on plasmonic nanostructures, metamaterials, and metasurfaces have been made for surface-enhanced spectroscopies, sensors, photovoltaics, super-resolution microscopy and lithography, metalenses, biomedical therapeutics, nonlinear optics, and integrated nanophotonics [1–3]. However, there are still significant material issues to be resolved such that plasmonics can be elevated to a transformative technology for general applications.

One critical issue of plasmonics is related to the intrinsic properties of available plasmonic materials. Nearly all of the research results adopt noble metals (silver [Ag] and gold [Au] are the most popular choices) as the plasmonic materials because they exhibit negative real and small imaginary parts of dielectric function in the visible and near-infrared spectral regions. However, noble metals suffer from high material cost (Au), low material stability (Ag), and incompatibility with existing semiconducting technology (Ag, Au). Furthermore, owing to the interband transitions in noble metals, spectral responses of plasmonic devices are limited in some specific ranges. To overcome these difficulties, alternative plasmonic materials, such as aluminum (Al), copper (Cu), transition metal nitrides, conducting metal oxides, and graphene have

*Corresponding author: Shangjr Gwo, Department of Physics, National Tsing-Hua University, Hsinchu 30013, Taiwan; Institute of NanoEngineering and Microsystems, National Tsing-Hua University, Hsinchu 30013, Taiwan; and Research Center for Applied Sciences, Academia Sinica, Nankang, Taipei 11529, Taiwan, E-mail: gwo@phys.nthu.edu.tw. https://orcid.org/0000-0002-3013-0477
Chang-Wei Cheng, Department of Physics, National Tsing-Hua University, Hsinchu 30013, Taiwan. https://orcid.org/0000-0001-8937-5084
Soniya S. Raja, Institute of NanoEngineering and Microsystems, National Tsing-Hua University, Hsinchu 30013, Taiwan
Ching-Wen Chang, Research Center for Applied Sciences, Academia Sinica, Nankang, Taipei 11529, Taiwan
Xin-Quan Zhang, Po-Yen Liu and Yi-Hsien Lee, Department of Materials Science and Engineering, National Tsing-Hua University, Hsinchu 30013, Taiwan
Chih-Kang Shih, Department of Physics, The University of Texas at Austin, Austin, TX 78712, USA

been extensively pursued in recent years [4–6]. Among them, aluminum is particularly interesting because it acts as an ideal Drude metal except a narrow interband transition window in the near-infrared (at 800 nm) [7]. In particular, for the ultraviolet (UV) and deep-UV plasmonic applications, aluminum is the best plasmonic material due to the negative real and relatively small imaginary parts of aluminum dielectric function in the UV region.

Considering practical applications, aluminum is also a sustainable plasmonic material since it is naturally abundant in the Earth's crust and has a native oxide protection layer (~3–5 nm Al_2O_3) [8, 9]. However, aluminum was not previously considered as a good candidate for alternative plasmonic material [5] before the advent of high-quality aluminum nanocrystals [10, 11] and epitaxial films [9, 12, 13] with greatly improved material properties. During the past few years, the fast development of aluminum plasmonics has attract a great deal attention not only for the expected good performance of aluminum for UV plasmonics, such as UV surface-enhanced Raman spectroscopy (UV-SERS) [14, 15], plasmonic lasers [16–22], and deep-UV resonances [8, 23], but also for its unexpected excellent performance in the visible region, including complementary metal-oxide-semiconductor (CMOS)-compatible color filters [24–28], photocatalysis [29], nonlinear optics [30–32], and SERS [15, 33]. Very recently, aluminum has even been found to outperform silver in some important plasmonic applications [15, 34].

The key to understand these finding is that the performance of plasmonic materials depends not only on their intrinsic optical properties but also their material properties, such as crystallinity, surface and interface quality, as well as stability. In the literature, aluminum nanostructures and metasurface are typically fabricated by lithographic methods using thermally evaporated aluminum films. In such cases, amorphous or polycrystalline film growth, as well as residual oxygen in the growth chamber, will eventually affect the performance of aluminum-based plasmonic devices. Recently, epitaxial aluminum film growth on commercially available substrates (silicon [13, 35, 36], GaAs [12, 37, 38], sapphire [9, 39, 40]) has been developed by using the molecular-beam epitaxy (MBE) technique under ultrahigh vacuum conditions. The availability of high-quality aluminum epitaxial films opens the way to explore aluminum plasmonics for real-world applications [8, 41, 42].

Here, we report on aluminum epitaxial films grown on sapphire substrates by MBE. This heteroepitaxial system is possible since the hexagonal lattice of Al (111) plane is close to that of the *c*-plane sapphire substrate (lattice mismatch is about 3.9%). Using these aluminum epitaxial films, we can have some distinct advantages for plasmonic applications, including high-fidelity nanofabrication for precise control of surface plasmon resonances owing to the single-crystalline material structure and large-scale, highly uniform plasmonic structures required for SERS substrates and high-quality-factor (high-Q) plasmonic surface lattices. Moreover, the aluminum film thickness is controllable down to a few atomic monolayers, allowing for ultrathin metal layer plasmonic applications [43–45]. It is worth noting that, since aluminum is considered as the "silicon" of superconductivity [46], aluminum epitaxial films can also be used as the building material for quantum computers requiring high-performance superconducting qubits.

2 Epitaxial growth and structural properties

Previous works on silver epitaxial films and nanostructures have demonstrated that crystalline properties and surface morphologies play an important role in plasmonic applications [47–53]. Especially, uniform and controllable plasmonic hot spots can realized by high-fidelity top-down nanofabrication on ultrasmooth, single-crystalline Ag colloidal crystals [53, 54]. In this work, aluminum epitaxial growth was conducted by using a MBE system under ultrahigh vacuum conditions. Two-inch double-side-polished *c*-plane sapphire (0001) wafers were used as the substrates, and the base vacuum pressure was kept about 1×10^{-10} Torr during growth. Before growth, the *c*-plane sapphire substrate was thermally cleaned at 950 °C for 2 h. A streaky reflection high-energy electron diffraction (RHEED) pattern of the *c*-plane sapphire surface can be obtained after this cleaning step (Figure 1A). Then, aluminum was evaporated by using a Kundsen cell. The deposition rate (about 200 nm/h) was controlled by the cell temperature, and the substrate temperature was maintained at room temperature (~300 K) during growth. A streaky RHEED pattern (Figure 1A) of aluminum film indicates a smooth film morphology during epitaxial growth.

The crystal orientation of epitaxial aluminum film was measured by X-ray diffraction (XRD) using the copper $K_{\alpha 1}$ line at the wavelength of 0.15406 nm. The XRD pattern (Figure 1B) shows the aluminum film is single-crystalline and grown along the (111) direction. The Al (111) and *c*-sapphire (0006) diffraction peaks are at about 38.5° and 42°, respectively. Due to the abrupt aluminum/sapphire interface and smooth film surface morphology, clear X-ray interference fringes of ultrathin aluminum films can be observed by high-resolution XRD (Figure 1B). Thus, we can

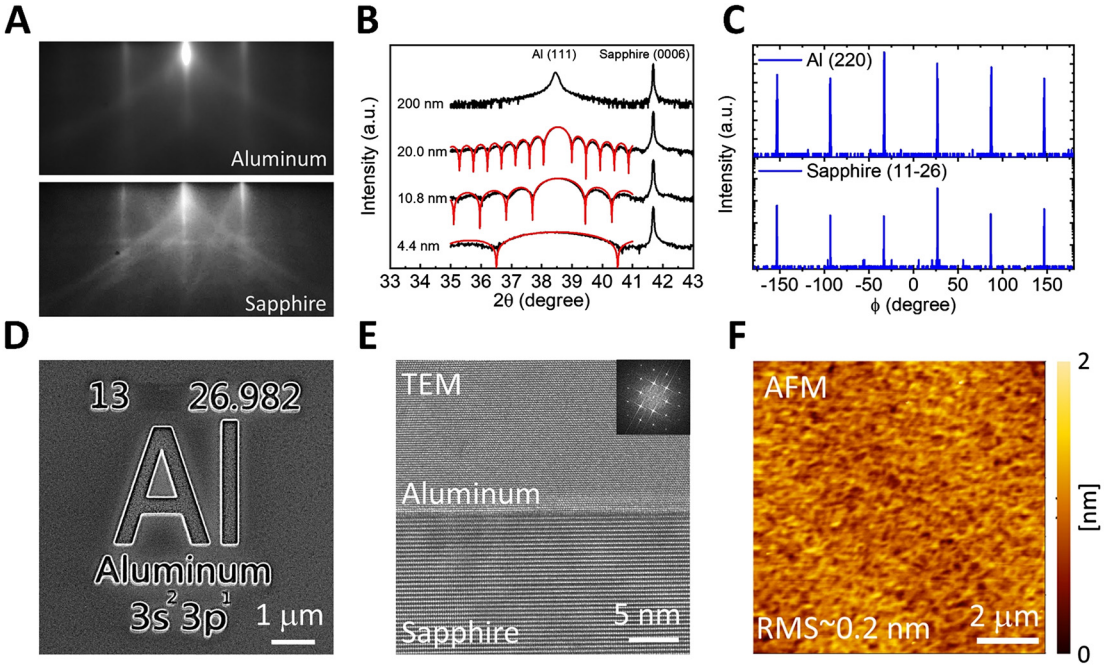

Figure 1: Structural properties of epitaxial aluminum films on sapphire substrates.
(A) In situ reflection high-energy electron diffraction (RHEED) patterns of *c*-plane sapphire and epitaxial aluminum film. (B) The X-ray diffraction patterns (2θ-scan) for 4.4 nm (~19 ML), 10.8 nm (~47 ML), 20.0 nm (~ 87 ML) and 200 nm-thick films, showing clearly the Al (111) peak, X-ray inference fringes, and the *c*-plane sapphire peak. The experimental data and the fitting curve are shown by black and red line, respectively. (C) The in-plane X-ray diffraction patterns (ϕ-scan) of Al (220) and *c*-sapphire (11–26) planes. (D) Scanning electron microscope (SEM) image of a focused ion beam patterned epitaxial aluminum. (E) High-resolution transmission electron microscope (TEM) image of an epitaxial aluminum film showing an abrupt interface between the epitaxial aluminum film and the *c*-sapphire substrate. The inset shows the fast Fourier transform of Al lattice along the [02-2] zone axis. (F) Atomic force microscope (AFM) image (10 × 10 μm^2) taken on the native oxide (~3 nm)-covered aluminum film. The film roughness is about 0.2 nm.

precisely determine the film thickness, ranging from a few nanometers, 4.4 nm (~19 monolayers [ML]), 10.8 nm (~47 ML), and 20.0 nm (~87 ML) to bulk-like (~200 nm). In Figure 1C, we show the in-plane X-ray diffraction scan performed for the Al (220) and *c*-sapphire (11–26) peaks, confirming the expected six-fold in-plane symmetry for epitaxial growth.

In Figure 1D, the scanning electron microscope image of a patterned aluminum epitaxial film (this pattern is adopted from an element periodic table) demonstrates that high-fidelity nanofabrication can be achieved via focused ion beam (FIB) lithography (FEI Helios NanoLab 600i) at an ion beam current of 7.7 pA due to the single-crystalline film properties. The high-resolution transmission electron microscope image (Figure 1E) shows the abrupt interface between the epitaxial aluminum film and the sapphire substrate. The root-mean-square (RMS) roughness of epitaxial aluminum film surface was measured by atomic force microscope (AFM), showing the RMS roughness of epitaxial aluminum film is atomically smooth (about 0.2 nm, Figure 1F).

3 Optical properties

The wafer scale epitaxial aluminum film is mirror-like (Figure 2A) due to a high optical reflectivity. We can compare the dielectric functions of literature data measured by spectroscopic ellipsometry (SE) for silver [51] and aluminum [9, 13] epitaxial films (Figure 2B and C). Previous studies have shown the Drude–Lorentz model can be used to fit dielectric functions of epitaxial silver and aluminum films [51, 55], which is expressed as

$$\varepsilon(\omega) = \varepsilon_1(\omega) + i\varepsilon_2(\omega) = \varepsilon_b - \frac{\omega_p^2}{\omega\left(\omega + i\gamma_p\right)} + \sum_{j=1}^{N} \frac{f_j \tilde{\omega}_j^2}{\left(\tilde{\omega}_j^2 - \omega^2 - i\omega\Gamma_j\right)}, \quad (1)$$

where ε_b is the polarization response from the core electrons (background permittivity), ω_p is the bulk plasmon frequency, γ_p is the relaxation rate (electron-electron scattering loss), f_j and $\tilde{\omega}_j$ are the strengths and resonant frequencies of interband transitions (N is the number of interband transitions used for modeling), and Γ_j is the

damping rates of interband transitions. In Figure 2C (inset), aluminum is clearly a better plasmonic material in the UV region compared to silver. In the following sections, we will show that epitaxial aluminum plasmonics can even be extended to cover the full visible spectral region.

Silver [51] and aluminum [13] epitaxial films with the best material quality were previously reported using a refined two-step growth process that shows the lowest optical loss. However, although the two-step growth technique can lead to superior film quality, it is a time-consuming process and growth conditions at cryogenic temperatures are difficult to achieve. Instead, room temperature and near-zero-Celsius-degree growth conditions are widely used for aluminum epitaxial films grown on high-quality commercial substrates (silicon [35, 36], gallium arsenide [37, 38], and sapphire [9]). There are two types of surface plasmons on these films: propagating surface plasmon polaritons (SPPs) and localized surface plasmons (LSPs). To compare the optical properties of epitaxial aluminum film between two different approaches [9, 13], we plot SPP (Q_{SPP}) and LSP (Q_{LSP}) quality factors in Figure 2D for both cases using the published data, where $Q_{SPP} = \frac{\mathrm{Re}(k_{SPP})}{\mathrm{Im}(k_{SPP})} \approx 2\frac{\varepsilon_1+\varepsilon_d}{\varepsilon_1\varepsilon_d}\frac{(\varepsilon_1)^2}{\varepsilon_2}$ [5] can be derived from the plasmon dispersion relation $k_{SPP} = \sqrt{\frac{\varepsilon_d\varepsilon(\omega)}{\varepsilon_d+\varepsilon(\omega)}}k_0 = n_{\mathrm{eff}}k_0 = \mathrm{Re}(k_{SPP}) + i\mathrm{Im}(k_{SPP}) = \frac{2\pi\,\mathrm{Re}(n_{\mathrm{eff}})}{\lambda} + \frac{2\pi\, i\mathrm{Im}(n_{\mathrm{eff}})}{\lambda}$ (ε_d is the dielectric constant of surrounding medium, $k_0 = \frac{2\pi}{\lambda}$ is the vacuum wavenumber, and n_{eff} is the SPP effective index) and Q_{LSP} can be expressed as $Q_{LSP} = \omega(d\varepsilon_1/d\omega)/2\varepsilon_2$ [56]. These comparison results indicate the optical properties of the room temperature–grown aluminum epitaxial films is indeed close to that grown by the two-step growth process.

4 Surface white light interface and plasmon propagation length

To demonstrate long SPP propagation length in the full visible spectral region, we fabricated surface double-groove structures by FIB milling. We measured SPP interference spectra using a white-light interference method [47–49, 52, 53] (WLI, Figure 3A). The incident SPPs are generated by a halogen light source with an oblique incident

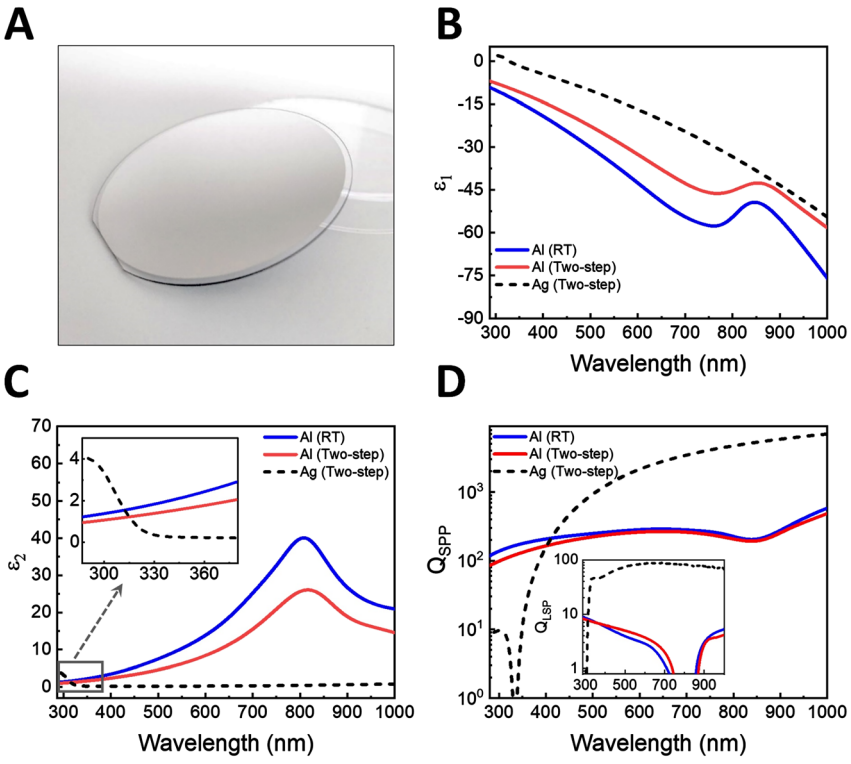

Figure 2: Optical properties of Al and Ag epitaxial films. (A) Optical image of Al epitaxial film on a 2-inch, *c*-plane sapphire substrate. (B) Real part of the dielectric function (ε_1) extracted from the literature data as a function of wavelength (blue solid curve). (C) Imaginary part of the dielectric constant (ε_2). For comparison, literature data of epitaxial Al (blue [9] and red line [13]) and Ag (black dash line [51]). The inset shows the wavelength from 287 to 380 nm. (D) The quality factor of SPP ($Q_{SPP} = \mathrm{Re}(k_{spp})/\mathrm{Im}(k_{spp}) \approx 2\frac{\varepsilon_1+\varepsilon_d}{\varepsilon_1\varepsilon_d}\frac{(\varepsilon_1)^2}{\varepsilon_2}$) comparison for Al and Ag epitaxial films. The inset shows the localized surface plasmons (LSP) quality factor ($Q_{LSP} = \omega(d\varepsilon_1/d\omega)/2\varepsilon_2$) comparison for Al and Ag epitaxial films.

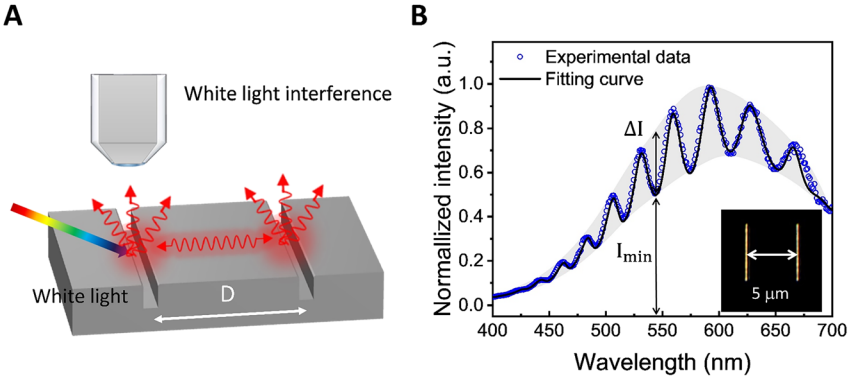

Figure 3: White-light surface plasmon interference. (A) Schematic of white-light interference method for measuring the surface plasmon polaritons (SPP) propagation length. (B) Scattering spectrum collected by the optical microscope objective. The inset is the optical scattering image from the double-groove structure. The groove separation (*D*) is 5 μm.

angle around 75–80° (see Supplementary material for experimental setup). The incident photons partially coupled to surface plasmons, which propagate along the aluminum surface covered with a 3-nm-thick native oxide (see Supplementary material for more details about the influence of oxide layer on optical properties). In order to reduce grain and surface scattering effects in the WLI measurements, single-crystalline and atomic-smooth aluminum surface are necessary, as reported in the previous works [47–49, 52, 53].

Figure 3B shows a clearly interference spectrum, indicating that propagating SPPs can reflect back and forth multiple times between two grooves. After multiple reflections and decoupling into far-field radiation at the incident groove, a microscope objective (100×, numerical aperture = 0.8) is used to collect the decoupled photons. The standard constructive and destructive interference conditions can be used to find the real part of SPP wave number

$$\begin{aligned} &\text{Peaks:}\ \ 2\mathrm{Re}\,(k_{SPP})D = 2q\pi \\ &\text{Dips:}\ \ 2\mathrm{Re}\,(k_{SPP})D = (2q+1)\pi\,, \end{aligned} \tag{2}$$

where D is the distance between two grooves, and q is an arbitrary integer number (q = 0, 1, 2, 3, …). In order to determine the exact q value and the real part of n_{eff}, we utilize the extracted dielectric function by SE in the long wavelength region for this purpose. After that, we can apply the Drude–Lorentz model (Eq. 1) to determine the imaginary part of n_{eff}. In general, the dielectric function acquired in this approach can match well with that determined by SE, and it has been confirmed for the present case of aluminum epitaxial film.

By using the conventional theory of Fabry–Pérot interferometry [57], we can further derive the electric field of scattered SPPs at the incident groove ($E_{SPP}(\lambda)$) as the following:

$$\begin{aligned} E_{SPP}(\lambda) &= \frac{\sqrt{I_{inc}(\lambda)}}{1 - R\exp(-2\mathrm{Im}\,(k_{SPP})D)\exp(2i\mathrm{Re}\,(k_{SPP})D)} \\ &= \frac{\sqrt{I_{inc}(\lambda)}}{1 - (RA)\exp(2i\mathrm{Re}\,(k_{SPP})D)}\,, \end{aligned} \tag{3}$$

where $I_{inc}(\lambda)$ is the incident SPP field intensity at the incident groove, R is the SPP reflectivity of both grooves, and $A \equiv \exp(-2\mathrm{Im}\,(k_{SPP})D) = \exp(-D/L_{spp})$ is the plasmonic propagation loss (absorption) factor between two grooves. Here, $L_{spp} \equiv 1/2\mathrm{Im}\,(k_{SPP}) = \lambda/4\pi\mathrm{Im}\,(n_{eff})$ is defined as the surface plasmon propagation length. According to Eq. (3), the ratio of interference maximum (I_{max}) and minimum (I_{min}) intensities can be expressed as the following:

$$\frac{I_{max}}{I_{min}} = \frac{\max\left(|E_{SPP}|^2\right)}{\min\left(|E_{SPP}|^2\right)} = \frac{(1+RA)^2}{(1-RA)^2} = \frac{(1+r)^2}{(1-r)^2}\,, \tag{4}$$

where $r \equiv RA$ is the round-trip reflectivity between two grooves, taking into account the plasmonic material loss. Furthermore, we can define the relative modulation depth [47]

$$\frac{\Delta I}{I_{min}} = \frac{I_{max} - I_{min}}{I_{min}} = \frac{4r}{(1-r)^2}\,, \tag{5}$$

where $\Delta I = I_{max} - I_{min}$ is the difference between the envelopes enclosing the intensity maxima and minima of the WLI pattern, and it indicates quantitatively how pronounced the SPP interference effect is.

In our measurements, $I_{max}(\lambda)$, $I_{min}(\lambda)$, as well as $r(\lambda)$ can be determined by experiment, as shown in Figure 3B. Furthermore, we can determine the values of A, L_{spp} and $R = r/A$ by using the dielectric function. Significant advantages of the WLI method are that we can directly correlate with the dielectric function determined by SE and measure the surface plasmon propagation lengths on the actual film surface in the full visible spectral range. As shown in Figure 3B, we can also numerically fit the experimental interference pattern with the following expression

$$I_{interference}(\lambda) = \frac{I_{max}(\lambda)(1-r)^2}{|1 - R\exp(4\pi i(n_{SPP})D/\lambda)|^2}\,, \tag{6}$$

where the fitting parameters R_{max} is found to be ~0.25 at 550 nm and L_{SPP} ranges from 5 to 13 μm in the spectral range of 400–700 nm. The plasmon propagation length

measured for the aluminum epitaxial film is comparable to that measured for single-crystalline silver nanowires at 785 nm (10 μm [47]).

5 Surface-enhanced Raman spectroscopy

Following the discussion of fundamental structural and optical properties, we now turn to the demonstration of epitaxial film–based plasmonic applications, including aluminum SERS substrate [15] and plasmonic surface lattices [22, 34, 58]. For the SERS study (see Supplementary material for experimental setup), we use a vertically stacked molybdenum disulfide (MoS_2)/tungsten diselenide (WSe_2) heterostructures on top of the aluminum SERS substrate (nanogroove grating) as a uniform two-dimensional analyte to evaluate the SERS performance (Figure 4A). The nanogroove array structure fabricated on the aluminum epitaxial film has the benefits of large-area spatial uniformity and wide-spectral tunability because of high-quality material properties.

The nanogroove array structure was fabricated by FIB milling for precise control of LSP resonance wavelength (plasmonic gap mode) via nanogroove grating dimensions (for the present case: width ~70 nm, depth ~110 nm, pitch ~250 nm). The Raman measurements were performed in the backscattering configuration using a 532-nm solid-state laser. Using this SERS substrate design [15], large-area chemical vapor deposition–grown MoS_2 and mechanically exfoliated WSe_2 stack on Al-SERS substrate can be clearly distinguishable (Figure 4B, D, and F) by Raman intensity mapping because of a spatially uniform Raman hot zone and atomically smooth film surface, which prevent the formation of inhomogeneous stochastic hot-spots.

In the Raman scattering spectra shown in Figure 4C and E, three prominent Raman active peaks can be identified with E^1_{2g} (384 cm^{-1}), A_{1g} (403 cm^{-1}), and $2LA(M)$ (447 cm^{-1}) vibrational modes, originating from monolayer MoS_2. On the other hand, a mixed Raman active

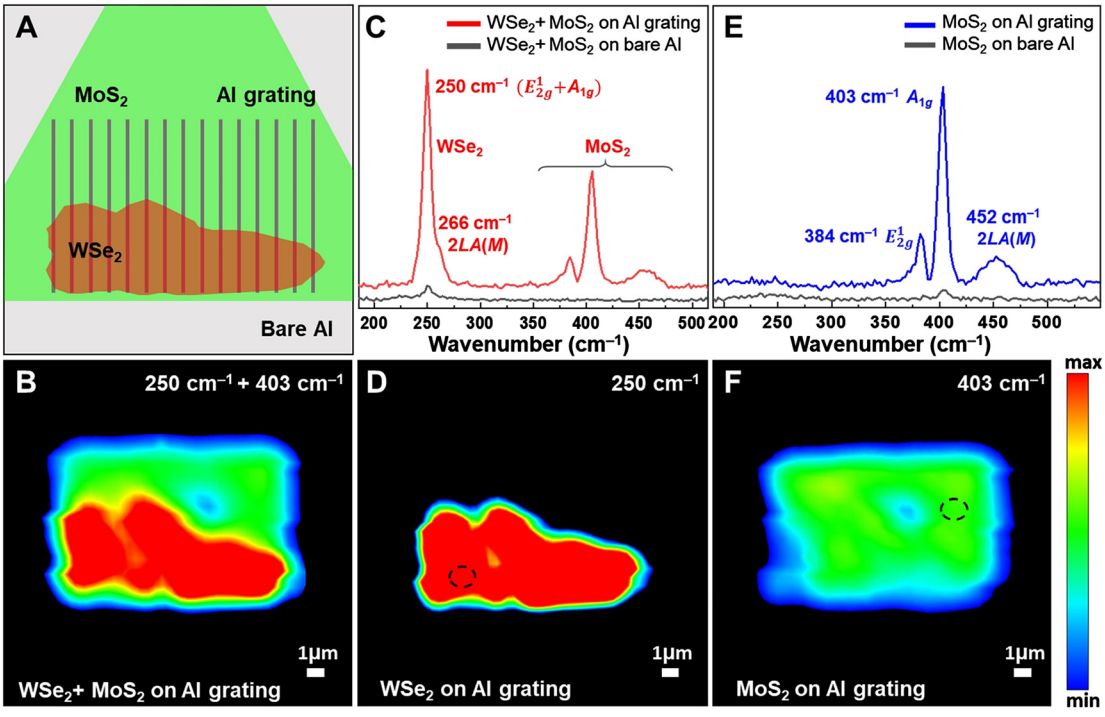

Figure 4: Raman intensity mapping of a vertically stacked monolayer transition metal dichalcogenide (TMDC) heterostucture. (A) Schematic of the surface-enhanced Raman spectroscopy (SERS) substrate structure, consisting of a grating with the size of 12 × 8 $μm^2$. The grating is sequentially stacked with MoS_2 and WSe_2 monolayers (WSe_2 on top). (B) Combining Raman intensity mapping of the A_{1g} peak (403 cm^{-1}) of MoS_2 monolayer and the $E^1_{2g} + A_{1g}$ mixed peak (250 cm^{-1}) of WSe_2 monolayer. The 532-nm excitation laser has a spot size ~2 μm, which limits the lateral resolution. (C) Enhanced Raman signals of MoS_2 and WSe_2 monolayers, which are recorded at the circled area in Figure 4D. The Raman signal of MoS_2 monolayer is still present since it is directly below the WSe_2 monolayer. (D) Raman intensity mapping at 250 cm^{-1}, corresponding to the $E^1_{2g} + A_{1g}$ mixed peak of WSe_2 monolayer. (E) Enhanced Raman signal of MoS_2 monolayer. (F) Raman intensity mapping at 403 cm^{-1}, corresponding to the A_{1g} peak of MoS_2 monolayer. The laser power density is ~30 kW/cm^2 and the exposure time is 1 s per data point. Scanning area is 20 × 20 $μm^2$.

peak $E^1_{2g} + A_{1g}$ (250 cm^{-1}) is identified for monolayer WSe_2. The E^1_{2g} and A_{1g} Raman peaks arise from the first-order, in-plane vibration of two S(Se) atoms relative to Mo(W) atom and out-of-plane vibration of S(Se) atoms, respectively. Due to the strong plasmonic field enhancement, we can also clearly observe the $2LA(M)$ peaks of MoS_2 (452 cm^{-1}) and WSe_2 (266 cm^{-1}), originating from a second-order process involving the longitudinal acoustic phonons at the M point of the Brillouin zone.

6 Plasmonic surface lattice

Generally, aluminum nanostructure dipolar resonators can only exhibit a small quality factor ($Q < 5$) due to a high radiative loss in the visible range [8, 11]. Here, we fabricate aluminum nanohole arrays (i.e., "antipartcle" arrays, in contrast to conventional nanoparticle arrays) on the aluminum epitaxial films as the plasmonic surface lattices to demonstrate high-Q plasmonic surface lattice [34, 58] modes based on propagating SPPs (the nanoholes are used

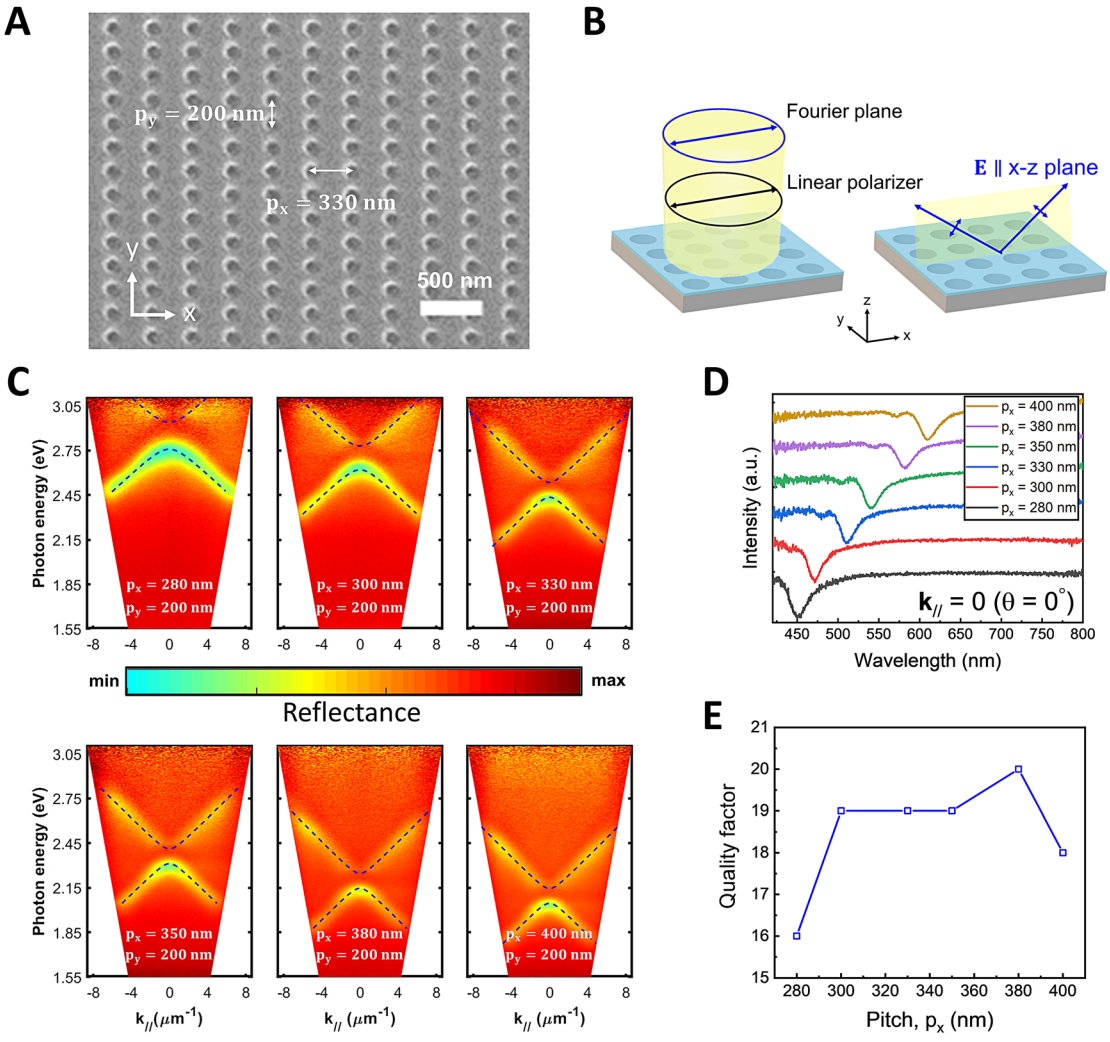

Figure 5: Optical properties of plasmonic surface lattices on epitaxial aluminum film. (A) Sample configuration of surface lattices patterned on epitaxial aluminum film. (B) Schematic of the optical setup for angle-resolved reflectance measurements, illustrating the orientations of spectrometer slit and polarizer with respect to the Al nanohole array capped with a polydimethylsiloxane (PDMS) layer. The Fourier spectra were collected by a 100× objective (N.A. = 0.55). (C) Angle-resolved reflectance mapping of the Al nanohole arrays, showing the evolution of the plasmonic surface lattice modes while the pitch along the x-axis (p_x) is increased from 280 to 400 nm. (D) Reflectance spectra of Al nanohole arrays extracted from the angle-resolved reflectance spectra (Figure 5C). All of resonance peaks are shown at the emission angle (θ) equal to 0°. (E) Measured quality factor of plasmonic surface lattice modes, which is defined as $Q = \lambda_{res}/\Delta\lambda$.

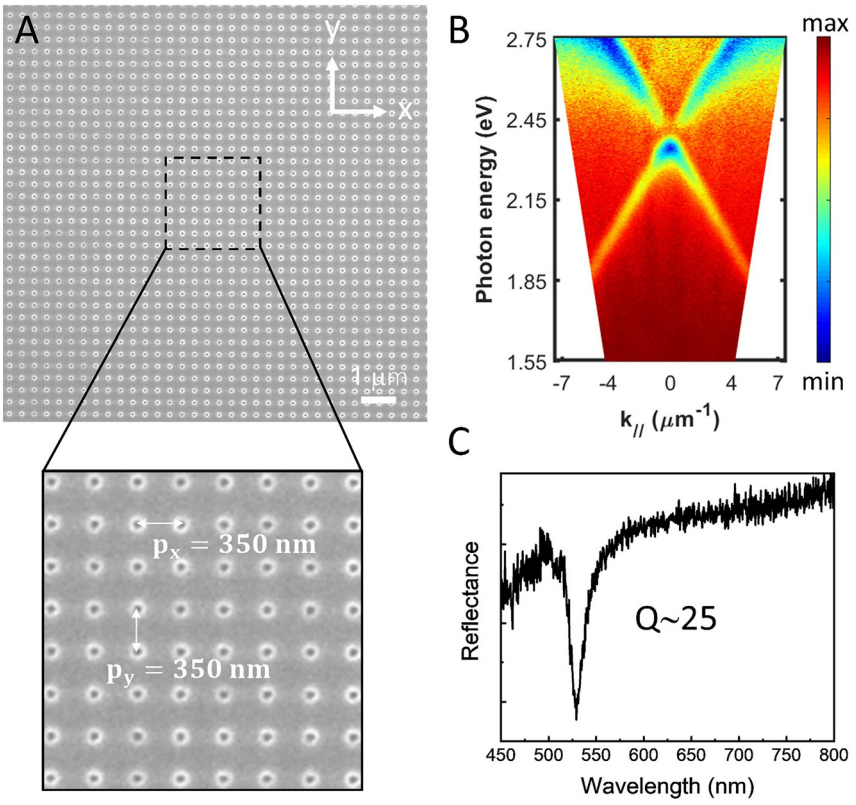

Figure 6: Optimization of aluminum nanohole surface lattice. (A) SEM image of the optimized aluminum plasmonic surface lattice. The inset shows the lattice constants (p_x and p_y) are 350 nm. (B) Angle-resolved reflectance mapping of the Al nanohole surface lattice. (C) Reflectance spectrum extracted from the angle-resolved reflectance mapping. The resonance peak is shown at the emission angle (θ) equal to 0°.

to define the spatial periodicities their LSP resonances do not play a significant role in these surface lattices). Since the nonradiative damping of plasmonic material is an intrinsic property originating from inter and intra band transitions, we focus on reducing the radiative loss by increasing the local effective index to enhance the near-field confinement factor. This is particularly important to realize high-Q plasmonic surface lattices based on SPPs. In this work, to improve the Q-factor, we cap one-mm-thick polydimethylsiloxane (PDMS) layer (refractive index: ~1.4) on the aluminum nanohole arrays to boost the effective index. The angle-resolved spectroscopic measurement results are shown in Figure 5, which is based on a back-focal-plane imaging technique (Figure 5B). In this setup, the angle-resolved spectra collect photons emitted by the aluminum plasmonic surface lattices along a specific emission angle with respect to the normal direction (see Supplementary material for experimental setup).

The nanohole arrays were fabricated by FIB milling on aluminum epitaxial film with different periodicities p_x = 280, 300, 330, 350, 380, 400 nm along the x-direction, while keeping a constant p_y = 200 nm, in order to tune the plasmonic surface lattice resonances at the Γ point of the lattice Brillouin zone. The angle-resolved reflectance spectra shown in Figure 5C illustrate the plasmonic surface lattice modes are well controlled by changing the pitch (p_x) and the filling factor of nanoholes. The reflectance spectra at the emission angle (θ) equal to 0° (Figure 5D) show the SPP resonance peaks, resulting from the band edge modes of plasmonic gaps at the Γ point, can be tuned in the entire visible range (from 450 to 600 nm). The Q-factor of plasmonic surface lattice modes (Figure 5E) can be evaluated by $\lambda_{res}/\Delta\lambda$, where $\Delta\lambda$ is the spectral linewidth (full width at half maximum) at resonance. Figure 5E shows the Q-factor can be improved to ~20 for this example. Using this method, we can design high Q-factor Al nanohole arrays over the entire visible spectral range, in comparison with colloidal aluminum nanoparticles [8, 11]. In addition, the plasmonic gap opening at the Γ point becomes very pronounced and we can produce both "dark" (subradiative) and "bright" (superradiative) band edge modes [59, 60], as shown in Figure 5C. Very recently, using more optimized nanofabrication conditions, a higher Q-factor aluminum surface lattice (shown in Figure 6) has also been realized by us (Q ~ 25, which is close to the theoretical limit reported in the literature for gold plasmonic surface lattices [61]).

7 Conclusions and outlook

In summary, we have demonstrated that epitaxial aluminum films are a promising material platform for

general plasmonic applications for both ultraviolet and visible spectral regions. White-light surface plasmon interferometry measurement in the entire visible range (400–700 nm) shows that long SPP propagation lengths (5–13 μm) can be achieved due to high-quality Al film. As the first example of plasmonic applications, the aluminum epitaxial film is used to fabricate large-area, highly uniform SERS substrates at 532 nm. A vertically stacked monolayer WSe_2/MoS_2 heterostructure is adopted as a uniform analyte to show the chemical mapping capability of SERS for two-dimensional material characterization. In the second application, large-area plasmonic surface lattices (periodic hole arrays) with precisely engineered lattice parameters are fabricated on an aluminum epitaxial film. By tuning the lattice parameter along one axis, we can control dark and bright band edge modes over the full visible spectrum. To improve the Q-factor of surface lattice modes, we cap the surface lattices with a PDMS dielectric layer to increase the local effective index. The Q-factor can be improved to ~25, compared to bare Al nanostructures without capping ($Q < 5$). The epitaxial approach reported here paves the way for widespread applications of aluminum plasmonics, especially for sensing, photonic system integration, and novel devices requiring ultrathin plasmonic layers. Moreover, it also can be applied for quantum information processing requiring high-quality aluminum superconducting qubits.

Acknowledgments: We would like to acknowledge funding support from the Ministry of Science and Technology in Taiwan for this research and Ragini Mishra for her help in XRD measurements. S.G. and Y.-H.L. were partially supported by Frontier Research Center on Fundamental and Applied Sciences of Matters at National Tsing-Hua University, the Featured Areas Research Center Program within the framework of the Higher Education Sprout Project by the Ministry of Education in Taiwan. C.-K.S was partially supported by the Yushan Scholar Program by the Ministry of Education in Taiwan.

Author contribution: All the authors have accepted responsibility for the entire content of this submitted manuscript and approved submission.

Research funding: This research was supported by the Ministry of Science and Technology in Taiwan under grants numbers MOST-108-2119-M-007-008 and MOST-107-2923-M-007-004-MY3.

Conflict of interest statement: The authors declare no conflicts of interest regarding this article.

References

[1] W. L. Barnes, A. Dereux, and T. W. Ebbesen, "Surface plasmon subwavelength optics," *Nature*, vol. 424, pp. 824–830, 2003.

[2] S. A. Maier and H. A. Atwater, "Plasmonics: localization and guiding of electromagnetic energy in metal/dielectric structures," *J. Appl. Phys.*, vol. 98, p. 011101, 2005.

[3] M. Khorasaninejad and F. Capasso, "Metalenses: versatile multifunctional photonic components," *Science*, vol. 358, p. eaam8100, 2017.

[4] I. Zorić, M. Zach, B. Kasemo, and C. Langhammer, "Gold, platinum, and aluminum nanodisk plasmons: material independence, subradiance, and damping mechanisms," *ACS Nano*, vol. 5, pp. 2535–2546, 2011.

[5] G. V. Naik, V. M. Shalaev, and A. Boltasseva, "Alternative plasmonic materials: beyond gold and silver," *Adv. Mater.*, vol. 25, pp. 3264–3294, 2013.

[6] B. Doiron, M. Mota, M. P. Wells, et al., "Quantifying figures of merit for localized surface plasmon resonance applications: a materials survey," *ACS Photonics*, vol. 6, pp. 240–259, 2019.

[7] H. Ehrenreich, H. R. Philipp, and B. Segall, "Optical properties of aluminum," *Phys. Rev.*, vol. 132, pp. 1918–1928, 1963.

[8] M. W. Knight, N. S. King, L. Liu, H. O. Everitt, P. Nordlander, and N. J. Halas, "Aluminum for plasmonics," *ACS Nano*, vol. 8, pp. 834–840, 2014.

[9] C. W. Cheng, Y. J. Liao, C. Y. Liu, et al., "Epitaxial aluminum-on-sapphire films as a plasmonic material platform for ultraviolet and full visible spectral regions," *ACS Photonics*, vol. 5, pp. 2624–2630, 2018.

[10] M. J. McClain, A. E. Schlather, E. Ringe, et al., "Aluminum nanocrystals," *Nano Lett.*, vol. 15, pp. 2751–2755, 2015.

[11] A. Sobhani, A. Manjavacas, Y. Cao, et al., "Pronounced linewidth narrowing of an aluminum nanoparticle plasmon resonance by Interaction with an aluminum metallic film," *Nano Lett.*, vol. 15, pp. 6946–6951, 2015.

[12] H. W. Liu, F. C. Lin, S. W. Lin, et al., "Single-crystalline aluminum nanostructures on a semiconducting GaAs substrate for ultraviolet to near-infrared plasmonics," *ACS Nano*, vol. 9, pp. 3875–3886, 2015.

[13] F. Cheng, P.-H. Su, J. Choi, S. Gwo, X. Li, and C.-K. Shih, "Epitaxial growth of atomically smooth aluminum on silicon and its intrinsic optical properties," *ACS Nano*, vol. 10, pp. 9852–9860, 2016.

[14] S. K. Jha, Z. Ahmed, M. Agio, et al., "Deep-UV surface-enhanced resonance Raman scattering of adenine on aluminum nanoparticle arrays," *J. Am. Chem. Soc.*, vol. 134, pp. 1966–1969, 2012.

[15] S. S. Raja, C.-W. Cheng, Y. Sang, et al., "Epitaxial aluminum surface enhanced Raman spectroscopy substrates for large-scale 2D material characterization," *ACS Nano*, vol. 14, pp. 8838–8845, 2020.

[16] Q. Zhang, G. Y. Li, X. F. Liu, et al., "A room temperature low-threshold ultraviolet plasmonic nanolaser," *Nat. Commun.*, vol. 5, p. 4953, 2014.

[17] Y.-H. Chou, Y.-M. Wu, K.-B. Hong, et al., "High-operation-temperature plasmonic nanolasers on single-crystalline aluminum," *Nano Lett.*, vol. 16, pp. 3179–3186, 2016.

[18] B.-T. Chou, Y.-H. Chou, Y.-M. Wu, et al., "Single-crystalline aluminum film for ultraviolet plasmonic nanolasers," *Sci. Rep.*, vol. 6, p. 19887, 2016.
[19] Y. Chou, K. Hong, Y. Chung, et al., "Metal for plasmonic ultraviolet laser: Al or Ag?," *IEEE J. Sel. Top. Quant. Electron.*, vol. 23, pp. 1–7, 2017.
[20] Y. J. Liao, C. W. Cheng, B. H. Wu, et al., "Low threshold room-temperature UV surface plasmon polariton lasers with ZnO nanowires on single-crystal aluminum films with Al_2O_3 interlayers," *RSC Adv.*, vol. 9, pp. 13600–13607, 2019.
[21] H. Li, J. H. Li, K. B. Hong, et al., "Plasmonic nanolasers enhanced by hybrid graphene-insulator-metal structures," *Nano Lett.*, vol. 19, pp. 5017–5024, 2019.
[22] R. Li, D. Wang, J. Guan, et al., "Plasmon nanolasing with aluminum nanoparticle arrays," *J. Opt. Soc. Am. B*, vol. 36, pp. E104–E111, 2019.
[23] G. Maidecchi, G. Gonella, R. P. Zaccaria, et al., "Deep ultraviolet plasmon resonance in aluminum nanoparticle arrays," *ACS Nano*, vol. 7, pp. 5834–5841, 2013.
[24] T. Xu, Y.-K. Wu, X. Luo, and L. J. Guo, "Plasmonic nanoresonators for high-resolution colour filtering and spectral imaging," *Nat. Commun.*, vol. 1, p. 59, 2010.
[25] S. Yokogawa, S. P. Burgos, and H. A. Atwater, "Plasmonic color filters for CMOS image sensor applications," *Nano Lett.*, vol. 12, pp. 4349–4354, 2012.
[26] J. Olson, A. Manjavacas, L. Liu, et al., "Vivid, full-color aluminum plasmonic pixels," *Proc. Natl. Acad. Sci. U.S.A.*, vol. 111, p. 14348, 2014.
[27] S. J. Tan, L. Zhang, D. Zhu, et al., "Plasmonic color palettes for photorealistic printing with aluminum nanostructures," *Nano Lett.*, vol. 14, pp. 4023–4029, 2014.
[28] D. Fleischman, K. T. Fountaine, C. R. Bukowsky, G. Tagliabue, L. A. Sweatlock, and H. A. Atwater, "High spectral resolution plasmonic color filters with subwavelength dimensions," *ACS Photonics*, vol. 6, pp. 332–338, 2019.
[29] L. Zhou, C. Zhang, M. J. McClain, et al., "Aluminum nanocrystals as a plasmonic photocatalyst for hydrogen dissociation," *Nano Lett.*, vol. 16, pp. 1478–1484, 2016.
[30] D. Krause, C. W. Teplin, and C. T. Rogers, "Optical surface second harmonic measurements of isotropic thin-film metals: gold, silver, copper, aluminium, and tantalum," *J. Appl. Phys.*, vol. 96, pp. 3626–3634, 2004.
[31] M. Castro-Lopez, D. Brinks, R. Sapienza, and N. F. van Hulst, "Aluminum for nonlinear plasmonics: resonance-driven polarized luminescence of Al, Ag, and Au nanoantennas," *Nano Lett.*, vol. 11, pp. 4674–4678, 2011.
[32] W. P. Guo, W. Y. Liang, C. W. Cheng, et al., "Chiral second-harmonic generation from monolayer WS_2/aluminum plasmonic vortex metalens," *Nano Lett.*, vol. 20, pp. 2857–2864, 2020.
[33] S. Tian, O. Neumann, M. J. McClain, et al., "Aluminum nanocrystals: a sustainable substrate for quantitative SERS-based DNA detection," *Nano Lett.*, vol. 17, pp. 5071–5077, 2017.
[34] X. Zhu, G. M. Imran Hossain, M. George, et al., "Beyond noble metals: high Q-factor aluminum nanoplasmonics," *ACS Photonics*, vol. 7, pp. 416–424, 2020.
[35] I. Levine, A. Yoffe, A. Salomon, W. J. Li, Y. Feldman, and A. Vilan, "Epitaxial two dimensional aluminum films on silicon (111) by ultra-fast thermal deposition," *J. Appl. Phys.*, vol. 111, p. 124320, 2012.
[36] Y. H. Tsai, Y. H. Wu, Y. Y. Ting, C. C. Wu, J. S. Wu, and S. D. Lin, "Nano-to atomic-scale epitaxial aluminum films on Si substrate grown by molecular beam epitaxy," *AIP Adv.*, vol. 9, p. 105001, 2019.
[37] S. W. Lin, J. Y. Wu, S. D. Lin, M. C. Lo, M. H. Lin, and C. T. Liang, "Characterization of single-crystalline aluminum thin film on (100) GaAs substrate," *Jpn. J. Appl. Phys.*, vol. 52, p. 045801, 2013.
[38] K. D. Zhang, S. J. Xia, C. Li, et al., "Interface engineering and epitaxial growth of single-crystalline aluminum films on semiconductors," *Adv. Mater. Interfaces*, p. 2000572, 2020. https://doi.org/10.1002/admi.202000572.
[39] Y. N. Zhu, W. L. Wang, W. J. Yang, H. Y. Wang, J. N. Gao, and G. Q. Li, "Nucleation mechanism for epitaxial growth of aluminum films on sapphire substrates by molecular beam epitaxy," *Mater. Sci. Semicond. Process.*, vol. 54, pp. 70–76, 2016.
[40] S. W. Hieke, G. Dehm, and C. Scheu, "Annealing induced void formation in epitaxial Al thin films on sapphire (α-Al_2O_3)," *Acta Mater.*, vol. 140, pp. 355–365, 2017.
[41] G. Davy and K. G. Stephen, "Aluminium plasmonics," *J. Phys. D Appl. Phys.*, vol. 48, p. 184001, 2015.
[42] C. J. DeSantis, M. J. McClain, and N. J. Halas, "Walking the walk: a giant step toward sustainable plasmonics," *ACS Nano*, vol. 10, pp. 9772–9775, 2016.
[43] R. A. Maniyara, D. Rodrigo, R. Yu, et al., "Tunable plasmons in ultrathin metal films," *Nat. Photonics*, vol. 13, pp. 328–333, 2019.
[44] B. Frank, P. Kahl, D. Podbiel, et al., "Short-range surface plasmonics: localized electron emission dynamics from a 60-nm spot on an atomically flat single-crystalline gold surface," *Sci. Adv*, vol. 3, p. e1700721, 2017.
[45] S. Campione, I. Brener, and F. Marquier, "Theory of epsilon-near-zero modes in ultrathin films," *Phys. Rev. B*, vol. 91, p. 121408, 2015.
[46] J. M. Martinis, M. H. Devoret, and J. Clarke, "Quantum Josephson junction circuits and the dawn of artificial atoms," *Nat. Phys.*, vol. 16, pp. 234–237, 2020.
[47] H. Ditlbacher, A. Hohenau, D. Wagner, et al., "Silver nanowires as surface plasmon resonators," *Phys. Rev. Lett.*, vol. 95, p. 257403, 2005.
[48] P. Nagpal, N. C. Lindquist, S.-H. Oh, and D. J. Norris, "Ultrasmooth patterned metals for plasmonics and metamaterials," *Science*, vol. 325, pp. 594–597, 2009.
[49] J. H. Park, P. Ambwani, M. Manno, et al., "Single-crystalline silver films for plasmonics," *Adv. Mater.*, vol. 24, pp. 3988–3992, 2012.
[50] Y.-J. Lu, J. Kim, H.-Y. Chen, et al., "Plasmonic nanolaser using epitaxially grown silver film," *Science*, vol. 337, pp. 450–453, 2012.
[51] Y. Wu, C. Zhang, N. M. Estakhri, et al., "Intrinsic optical properties and enhanced plasmonic response of epitaxial silver," *Adv. Mater.*, vol. 26, pp. 6054–6055, 2014.
[52] F. Cheng, C.-J. Lee, J. Choi, et al., "Epitaxial growth of optically thick, single crystalline silver films for plasmonics," *ACS Appl. Mater. Interfaces*, vol. 11, pp. 3189–3195, 2019.
[53] C. Y. Wang, H. Y. Chen, L. Y. Sun, et al., "Giant colloidal silver crystals for low-loss linear and nonlinear plasmonics," *Nat. Commun.*, vol. 6, p. 7734, 2015.
[54] S. Gwo, H.-Y. Chen, M.-H. Lin, et al., "Nanomanipulation and controlled self-assembly of metal nanoparticles and

nanocrystals for plasmonics," *Chem. Soc. Rev.*, vol. 45, pp. 5672–5716, 2016.
[55] A. D. Rakic, A. B. Djurisic, J. M. Elazar, and M. L. Majewski, "Optical properties of metallic films for vertical-cavity optoelectronic devices," *Appl. Opt.*, vol. 37, pp. 5271–5283, 1998.
[56] F. Wang and Y. R. Shen, "General properties of local plasmons in metal nanostructures," *Phys. Rev. Lett.*, vol. 97, p. 206806, 2006.
[57] B. E. A. Saleh and M. C. Teich, *Fundamentals of Photonics*, New York, John Wiley & Sons, 1991.
[58] V. G. Kravets, A. V. Kabashin, W. L. Barnes, and A. N. Grigorenko, "Plasmonic surface lattice resonances: a review of properties and applications," *Chem. Rev.*, vol. 118, pp. 5912–5951, 2018.
[59] S. R. K. Rodriguez, A. Abass, B. Maes, O. T. A. Janssen, G. Vecchi, and J. Gómez Rivas, "Coupling bright and dark plasmonic lattice resonances," *Phys. Rev. X*, vol. 1, p. 021019, 2011.
[60] T. K. Hakala, H. T. Rekola, A. I. Väkeväinen, et al., "Lasing in dark and bright modes of a finite-sized plasmonic lattice," *Nat. Commun.*, vol. 8, p. 13687, 2017.
[61] S. R. K. Rodriguez, M. C. Schaafsma, A. Berrier, and J. Gómez Rivas, "Collective resonances in plasmonic crystals: size matters," *Phys. B Condens. Matter*, vol. 407, pp. 4081–4085, 2012.

Supplementary Material: The online version of this article offers supplementary material (https://doi.org/10.1515/nanoph-2020-0402).